Acta Biomaterialia 15 (2015) 244–253

Contents lists available at ScienceDirect

Acta Biomaterialia

journal homepage: www.elsevier.com/locate/actabiomat

Damage modeling of small-scale experiments on dental enamel with hierarchical microstructure

I. Scheider [a,*], T. Xiao [a], E. Yilmaz [c], G.A. Schneider [c], N. Huber [a], S. Bargmann [a,b]

[a] Institute of Materials Research, Materials Mechanics/ACE-Centre, Helmholtz-Zentrum Geesthacht, Germany
[b] Institute of Continuum Mechanics and Materials Mechanics, Hamburg University of Technology, Germany
[c] Institute of Advanced Ceramics, Hamburg University of Technology, Germany

ARTICLE INFO

Article history:
Received 17 July 2014
Received in revised form 27 October 2014
Accepted 18 November 2014
Available online 5 December 2014

Keywords:
Dental enamel
Mechanical characterization
Micromechanical modeling
Hierarchical material
Homogenization

ABSTRACT

Dental enamel is a highly anisotropic and heterogeneous material, which exhibits an optimal reliability with respect to the various loads occurring over years. In this work, enamel's microstructure of parallel aligned rods of mineral fibers is modeled and mechanical properties are evaluated in terms of strength and toughness with the help of a multiscale modeling method. The established model is validated by comparing it with the stress–strain curves identified by microcantilever beam experiments extracted from these rods. Moreover, in order to gain further insight in the damage-tolerant behavior of enamel, the size of crystallites below which the structure becomes insensitive to flaws is studied by a microstructural finite element model. The assumption regarding the fiber strength is verified by a numerical study leading to accordance of fiber size and flaw tolerance size, and the debonding strength is estimated by optimizing the failure behavior of the microstructure on the hierarchical level above the individual fibers. Based on these well-grounded properties, the material behavior is predicted well by homogenization of a representative unit cell including damage, taking imperfections (like microcracks in the present case) into account.

1. Introduction

Nature has showcased the possibility of combining brittle minerals and organic proteins into composites with remarkably increased fracture resistance. Taking dental enamel as an example, the content of hydroxyapatite (HAp) is up to 96 wt.%, with the remaining portion composed of protein and water [1]. However, HAp has been limited to non-load-bearing biomedical/clinical applications because of its poor fracture resistance [2]. The reason for the significant increase toughness of biological HAp-based composites remains unresolved [3]. The general aim of the systematic characterization and investigation of existing hierarchical natural materials is to promote new ways to synthesize composite materials with equally remarkable mechanical properties.

Gao et al. [4] suggested that the impressive behavior of mineralized biological materials is due to nanometer confinement of mineral crystallites based on the theory that mineral crystallites become flaw-tolerant at the nanometer length scale. This concept has been confirmed by experimental work [5,6] which demonstrates that simultaneous improvement of hardness and toughness can be attained purely by decreasing the grain size of HAp from submicrometers to nanometers. Moreover, nanosized mineral crystallites also enable enamel having the largest hardness, as indicated, for example, by Refs. [7–9].

Enamel is usually characterized by experiments as a three-level hierarchical structure, which spans from the nanoscaled to the macroscaled level [10]; however, the hierarchical terminology was originally introduced by Koenigswald and Clemens [11], who identified up to seven hierarchical levels. The considerable amount of work published about enamel has focused on characterizing the mechanical properties either at the macroscale (millimeter) or at the nanometer scale, without taking into consideration the various hierarchical levels in the sample. That causes a large discrepancy in terms of measured hardness, elastic modulus and fracture toughness, which makes elucidation of its true structure–property relationship even more challenging [12–15]. More recently, there is an emerging interest in the role of hierarchical design by identifying the enamel's mechanical properties at each hierarchical level [7,16,17]. These works clearly reveal that nature enables enamel to possess a damage-tolerant behavior by increasing the number of hierarchy levels.

The properties of enamel depend on its position within the tooth and geometry of the sample. Consequently, there is a large variation with respect to the mechanical properties reported in

* Corresponding author.

http://dx.doi.org/10.1016/j.actbio.2014.11.036
1742-7061/

the literature. This uncertainty is an obstacle for better understanding the structure–property relationship of enamel solely using experimental characterization. Thorough understanding of the design principles and mechanical properties of enamel can only be achieved through development of analytical and computational models along with the experimental investigations. A pioneering theoretical model capable of predicting the strength, stiffness and toughness at each level of hierarchy was proposed by Gao [18] for self-similar hierarchical assemblies. This simplified model provides the fundamental design principle of hierarchical materials. Zhang et al. [19] extended this model by applying an elastic–plastic model to evaluate the optimal number of hierarchy levels for biomaterials, without accounting for damage.

Sen and Buehler [20] developed mesoscale molecular mechanics based models to investigate the failure behavior of hierarchical materials. Their models demonstrated the two toughening mechanisms of bone-like and biocalcite-like structures, and exemplified the potential of obtaining materials with superior mechanical properties despite the use of a single brittle constituent through the use of hierarchical structure. Compared to the large number of models dedicated to study the hierarchical microstructure of bone, there are only a limited number concerned with that of enamel. Micromechanical modelling of staggered biocomposites was also employed using representative microstructures by other groups (see e.g. Ref. [21]).

The very first micromechanical simulation of dental enamel by Spears [22] investigated the Young's modulus based on an assembly of rods of mineral fibers. Bar-On and Wagner [23] presented an analytical multiscale mechanical model for estimating the effective elastic modulus of enamel. An et al. [24] developed a micromechanical model of enamel prism to examine the effect of HAp crystallite orientation on the plastic deformation behavior of enamel. Bargmann et al. [25] formulated a thermodynamically consistent model for the material behavior of enamel, with an emphasis on capturing the failure mechanisms of enamel on the nanoscaled structure. This selection of works shows that, even though the theoretical basis for numerical modeling is quite mature, only the elastic properties are usually homogenized for an efficient modeling of a larger portion of a hierarchical material like dental enamel. Improvement to the existing models can be achieved by taking the effects of material anisotropy and interface properties into account. The modeling of damage across several scales is highly sophisticated; however, the link from microstructural modeling to structural simulations of fracture in a complete tooth, as conducted, for example, in Ref. [26], is still missing. Further, to the best of the authors' knowledge, all existing models propose the type of damage (breaking, debonding, etc.) that occurs in the material as input to their simulations – with the exception of our earlier work [25], which is further extended in this contribution.

In our previous work we proposed a continuum mechanics based modeling approach for addressing the size effect as well as the interactions of heterogeneous structure in composites [27,28]. The failure behavior of enamel on the nanoscale has been predicted [25], the size effect in nanoindentation tests has been studied [7] and the influence of HAp fiber orientation on the stiffness of the enamel has been investigated. Here, we employ the idea of a bottom-up hierarchical structure and realize a complete scale separation in modeling in order to fill the gap between micromechanical based modeling and the future structural simulation of tooth fracture.

2. Dental enamel microstructure and its numerical representation

2.1. Experimental characterization

The microstructure of the dental enamel of all mammals (including humans) is assembled on several hierarchy levels according to Ref. [11]. The lowest level that is of interest here (referred to in the following as level 1) is the fibrous composite that consists of unidirectionally aligned HAp fibers surrounded by a small protein interlayer (see Fig. 1a, taken from bovine tooth material). Hydroxyapatite is a strong but brittle mineral, while the

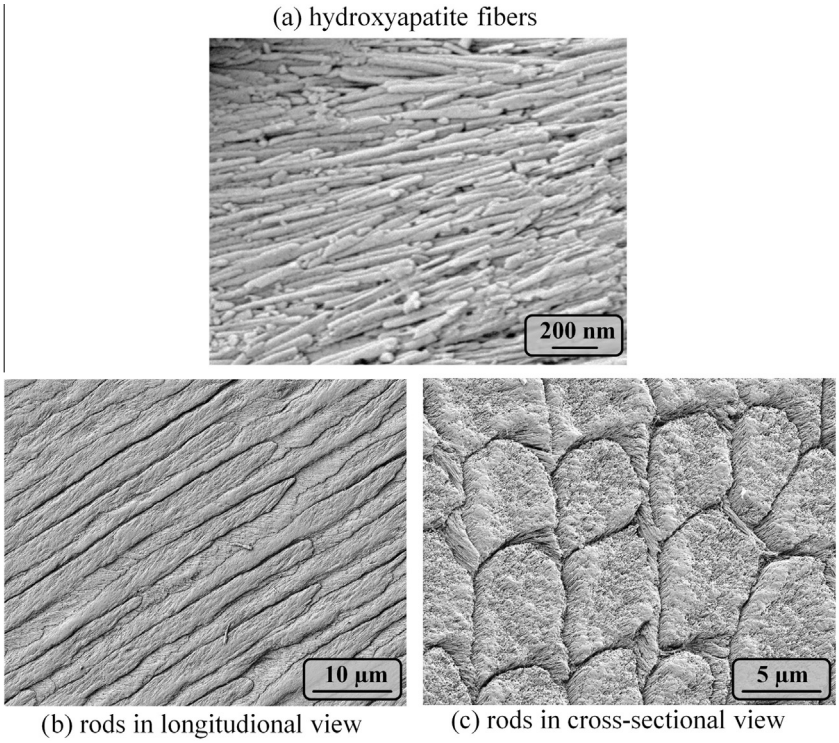

Fig. 1. Microstructure of bovine dental enamel (similar to that of all mammals).

protein is roughly 100 times softer (in terms of Young's modulus). The diameter of the fibers is approx. 30–50 nm [29,30]. A definite value of their length is still under discussion, but it is generally accepted that they are very long, maybe even 100 μm or longer [31]. The volume fraction of the mineral is about 90%.

The fiber-reinforced microstructure is arranged in larger rods in the dental enamel (see Fig. 1b and c). Again, a thin protein interlayer connects the rods, such that the rod volume is again approx. 90% of the total volume; that is, the material is self-similar on these two hierarchy levels. Further information regarding the hierarchy and microstructural features of enamel is beyond the scope of this work; therefore, readers are referred to Ref. [11,10] for more details.

2.2. Material modeling

In the numerical simulations, the microstructure is represented by a number of mineral fibers surrounded by a protein matrix interlayer. Due to the very high fiber volume fraction, it is necessary to use a prismatic cross-section, which allows for any fiber content up to 100%. In the following, fibers with hexagonal cross-sections are used.

The material models for two components, HAp and protein, which are the basic constituents of dental enamel, have already been outlined in Ref. [25] and will be mentioned only briefly here. Emphasis is placed on the material model used for the deformation of the homogenized material to be used on the second hierarchy level later on.

2.2.1. Deformation

As the Hydroxyapatite fibers are brittle and very stiff, they experience only small strains. The deformation of this material is described by a hyperelastic model of neo-Hookean type, the damage by a cohesive zone at predefined planes. The parameters used for the HAp fibers are the same as those employed in Ref. [25], i.e. the Lamé constants are $\lambda = 27700$ MPa and $\mu = 32520$ MPa.

The protein matrix material is roughly 100 times softer than the fiber. According to the literature, the nonlinear elastic material behavior of the nearly incompressible protein can be captured by the Arruda–Boyce model [32,33]. The constitutive equations have been given in Ref. [25]; the three necessary parameters used here are the same as before: $\mu_0 = 301$ MPa, $K_0 = 30000$ MPa and the so-called locking stretch $\lambda_m = 1$.

The model of any hierarchy level with a substructure contains the information of the previous level. However, the microstructure of such fibers is modeled in a homogenized fashion, so that the composite microstructure is represented by one material model. The homogenization strategy is explained in detail in Section 4.

2.2.2. Damage

In addition to deformation, damage is captured in the simulations. This is done by employing cohesive zone elements in the fibers, in the protein matrix and at the physical interfaces between the fiber and the matrix material, as has also been presented in Ref. [25]. Allowing for three different damage regions is important for capturing various failure mechanisms, as it has already been shown in Ref. [25,27]. The constitutive behavior of the cohesive model is taken from Ref. [34] with a damage evolution law, leading to a linearly decreasing traction after damage initiation for the HAp, the protein and the interface in-between (the elastic stiffness is set to a high value so that the deformation in the interfaces remain small). The two characteristic parameters in each of these regions are the cohesive strength and the fracture energy. In the present investigation, we start with the parameters used in Ref. [25], which were taken from the literature, but will discuss and adjust them according to the optimal behavior of the microstructure in Section 3.

The traction–separation law for the composite, which is used on higher hierarchy levels, is developed from the homogenization results and will be presented in Section 4.

3. Simulation of the first hierarchy level

3.1. Model setup

In this section, a small portion of the microstructure representing the main features of the composition is described numerically by finite element simulations. It contains several mineral fibers and the protein–matrix interlayer, and is denoted in the following as a representative unit cell. In the present case, this representative unit cell (RUC; cf. Fig. 2) consists of fibers with an aspect ratio (length over diameter) of 20, which has benn proven to correspond to experimental data on level 1 (see [25]). The fibers have a hexagonal cross-section so that the volume fraction can be increased to 100%. Four fibers are included in the model and all fibers end at different positions in the unit cell. The light grey region in Fig. 2 depicts the protein matrix, while the green (or dark in the black & white print) region shows the fibers. The fiber ends are visible from the thin intersections. The displacement of the surfaces of the unit cells are constrained by periodic boundary conditions.

From the structural response of such a unit cell undergoing mechanical loading, the material behavior on the next higher level can be retrieved by numerical homogenization, as will be outlined in the following section.

An idealized microstructure is assumed. However, its theoretical strength is not reached in real structures, since stochastic effects originating from various sources play a major role. There may be local variations in fiber diameter, fiber orientation, fiber volume fraction, fiber wrinkling and other irregularities, and material properties. Further, several kinds of degrading effects may occur, such as flaws, impurities and finite fiber sizes. These complex features cannot be taken into account by the rather simple unit cell modeled here. In order to respect any irregularities, a flaw

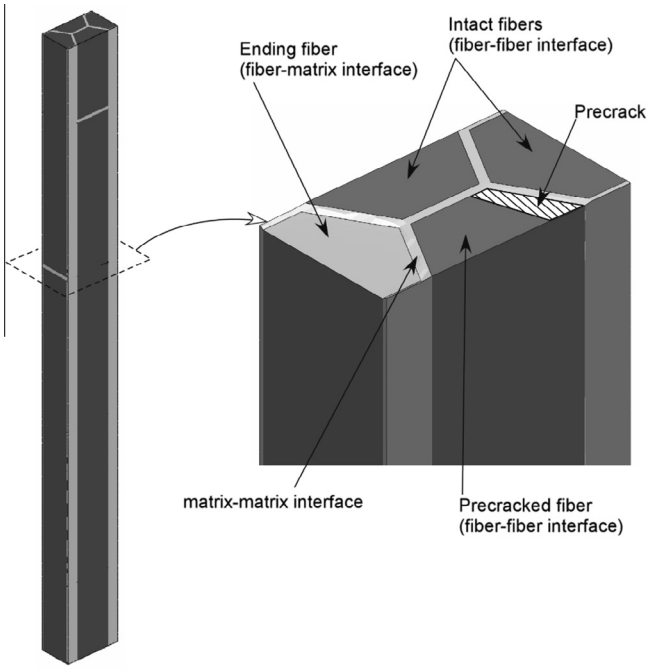

Fig. 2. RUC with one precracked fiber at the worst position for a tensile loading in fiber direction, i.e. in the plane where another fiber ends.

has been included in the model, that is, one fiber is precracked by 25% of its original cross-section (see Fig. 2). The size of the precrack is arbitrary, as is the position of the crack. The worst case for a position under tensile loading in the fiber direction is naturally close to an end of another fiber. Accounting for the fiber being small enough to become flaw tolerant according to Gao's analytical consideration ([18,16]), the flaw does not reduce the strength of the representative unit cell significantly, the difference in strength being approx. 9%.

3.2. Discussion on cohesive model parameters

According to a simple rule of mixture based on strain equivalence, which is valid for unidirectional infinitely long fibers, the theoretical strength, σ^{theor}, and the fracture energy, Γ^{theor}, of the fiber-reinforced composite loaded in fiber direction can be calculated by:

$$\begin{aligned}\sigma^{\text{theor}} &= T_0^{\text{HAp}} f^{\text{HAp}} + T_0^{\text{Prot}} f^{\text{Prot}} \\ \Gamma^{\text{theor}} &= \Gamma_0^{\text{HAp}} f^{\text{HAp}} + \Gamma_0^{\text{Prot}} f^{\text{Prot}}\end{aligned} \tag{1}$$

with T_0, Γ_0 being the cohesive strength and energy of the HAp fibers and the protein, and f the corresponding volume fractions, respectively.

3.2.1. Protein cohesive strength

The strength of the protein is of minor importance due to the very small volume fraction of protein, hence this value is not discussed in detail. Simple mathematics shows that the results differ only slightly if this strength is changed. The cross-section of the protein is approx. 10% of the total cross-section, and the cohesive strength is also only in the order of 10% of the fiber strength. Therefore, if only protein were to carry the load, the total strength of the microstructure would be 1% of the actual strength. Since a protein strength of more than 300 MPa has never been reported in the literature, we assume $T_0^{\text{prot}} = 200\,\text{MPa}$, which is a rather high assumed value, and decreasing this value further does not deter the microstructural strength appreciably.

3.2.2. Mineral cohesive strength

The diameter of the HAp fibers is approximately 50 nm. According to semi-analytical considerations with respect to a flaw-tolerant microstructure conducted by Gao [18], nature has chosen the size to be that small because a characteristic size of microstructural entities exists, below which even a precracked particle/fiber can withstand stresses up to its theoretical strength. This characteristic length is called the flaw-tolerance size h_{ft}, which, according to Gao[1], can be calculated by the following equation:

$$h \leqslant \frac{G_c E}{[\sigma_c]^2} = h_{\text{ft}} \tag{2}$$

with G_c being the fracture toughness (critical strain energy), E the Young's modulus and σ_c the maximum strength of the entity. Together with the parameters used in Ref. [25] for the fibers, $G_c = \Gamma_0^{\text{HAp}} = 10\,\text{J/m}^2, \sigma_c = T_0^{\text{HAp}} = 2000\,\text{MPa}$ and the elastic modulus $E^{\text{HAp}} = 80\,\text{GPa}$, this actually leads to a flaw-tolerant size of $h_{\text{ft}} = 0.2\,\mu\text{m}$.

Eq. (1) leads to $\sigma_0^{\text{theor}} = 1820\,\text{MPa}$. Simulations with different fiber sizes and one precracked fiber[2] show that the strength of 1820 MPa is reached for fibers having an equivalent diameter of 60 nm or less (see Fig. 3). This corresponds very well with the actual size of the HAp fibers in the dental enamel shown in Fig. 1, that is, the model supports nature's choice for its microstructural entities.

3.2.3. Debonding strength

Due to the small scale of the HAp fibers, it is hardly possible to characterize the debonding interface experimentally. Dastjerdi et al. [35] attempted to identify the debonding properties of a similar material, namely the microstructure of fish scales, using a combined experimental–numerical investigation, leading to a cohesive traction–separation law. Here, a different, purely numerical approach is employed.

Biological composites, like any fiber-reinforced composite, can fail due to fiber breaking or debonding – or a mixture of both. Gao [18] reported that the resistance against debonding and breaking should be in equilibrium. Consequently, the debonding strength must be adjusted to the point where the debonding failure mode flips into the breaking failure mode. This can only be done numerically. However, such numerical investigations for biological materials are rare; RUCs were used in combination with the cohesive model for platelet microstructures in Ref. [36]. In our previous work [25], where a similar unit cell as the one shown in Fig. 2 was employed, we showed that fibers with an aspect ratio higher than 6 will break rather than debond. The model used in this investigation differs from the one used in Ref. [25] in the sense that now the stress distribution is much more inhomogeneous due to the precrack in one fiber. Therefore not only can two failure modes be distinguished under tensile loading in the fiber direction, but there may be the following failure modes:

- pure debonding
- breaking of the precracked fiber and debonding of the others
- breaking of the precracked fiber and one other fiber, debonding of one fiber
- pure breaking

Any of these failure modes can be achieved by varying the debonding strength. However, microstructural fracture tests indicate that debonding is a dominant failure mode: the fracture surface of a broken microcantilever beam (see Fig. 4) documents that many HAp fibers are pulled out. The length of these fiber parts that is

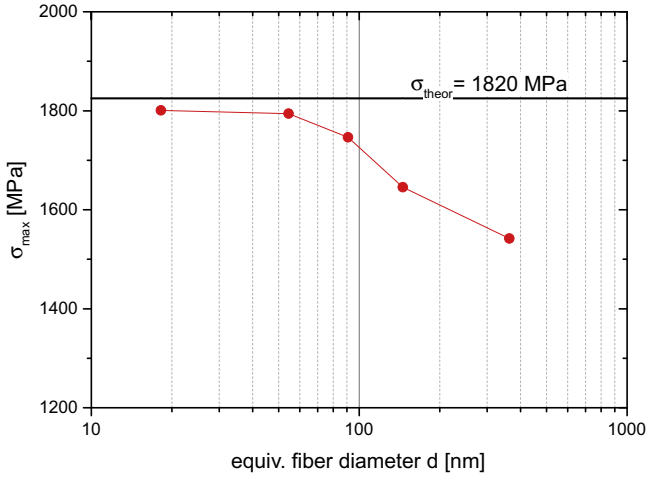

Fig. 3. Maximum strength vs. diameter of the fiber (the fiber's dimensions are scaled uniformly). The theoretical strength is reached for fibers with an equivalent fiber diameter smaller than or equal to 60 nm.

[1] In the investigation performed by Gao, a center-cracked platelet has been considered.

[2] In these simulations, fiber breaking is enforced and fiber ends are not taken into account. Therefore the model is different from the one shown in Fig. 2. The finite element model is given in Ref. Appendix A.

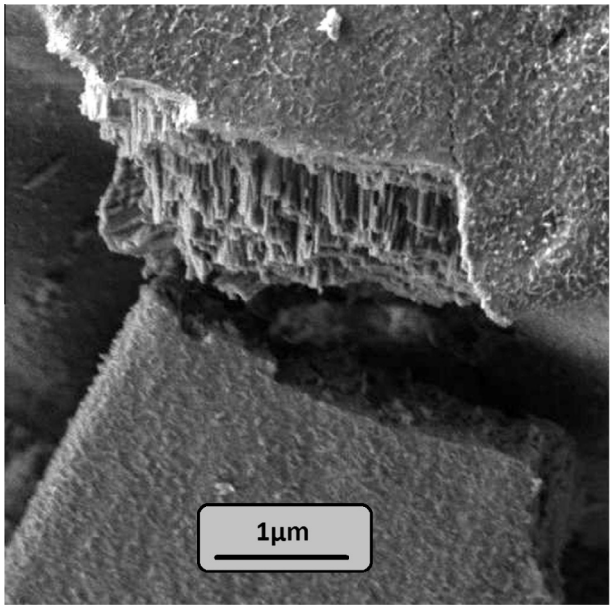

Fig. 4. Fracture surface of the cantilever beam fabricated within a single rod representing the first level of hierarchy, showing significant debonding of the HAp fibers.

visible is incidentally in the range of the fibers used in our representative unit cell simulations.

In order to study the debonding strength, this parameter has been varied in the range $T_0^{\mathrm{deb}} = [30 \ldots 200]$ MPa with constant fracture energy $\Gamma_0 = 100\,\mathrm{J/m^2}$. The reason for such a wide variation is the phenomenological interpretation of debonding strength identified by a continuum mechanics based approach that may also involve local dissipation through inelastic processes near to the crack tip. With this study, we aim to reproduce the effects visible in the experiment, assuming that microscopic phenomena are sufficiently represented in the homogenization of the cohesive zone model, which includes the interface and the surrounding material. The results are shown in Fig. 5. For a debonding strength of 150 MPa or higher, breaking is the predominant failure mechanism. The corresponding stress–strain curves contain a high stress peak followed by a sharp drop due to the strength and brittleness of the fiber – a behavior which is typical for composite materials. When the mineral fibers fail completely, the protein matrix material can still sustain some (much lower) stresses up to significantly higher strains. Fig. 5 shows that the maximum strength of a precracked representative unit cell is $\sigma_{\max} = 1230$ MPa, which is approx. 12% lower than the strength of an uncracked specimen. If the debonding strength is decreased to 80–120 MPa, the precracked and one uncracked fiber are breaking, while one fiber is debonding. The maximum strength is decreased slightly; however, a higher stress level remains when the fibers have totally failed, which leads to a higher overall fracture energy of the composite material.

For an even lower debonding strength of 60 MPa, debonding of all fibers, including the precracked fiber, occurs. This failure mechanism is characterized by a further decrease in strength of the composite microstructure, but the maximum stress level remains high up to very high strain levels and then decreases linearly to zero. In Fig. 5 this failure mechanism is visible for 60 and 30 MPa.

Regarding the cohesive energy of the debonding interface, it is worth mentioning that it does not significantly affect either the maximum stress of the representative unit cell or the fracture mechanism itself. However, the softening branch in the case of a debonding fracture mechanism changes and thus so does the overall energy dissipated by the microstructure (see also Ref. [28]). These simulations support the conclusion that the debonding strength should be approximately $T_0^{\mathrm{deb}} = 60$ MPa – but the debonding energy cannot be ascertained here. That discussion is therefore be postponed to the experimental validation Section 5.

4. Homogenization strategy

The simulation of the hierarchical aggregation of the enamel microstructure is based on the assumption that the composition of fibers with surrounding protein has the same structure on every hierarchy level, i.e. the structure is self-similar (see Fig. 6). Even though dental enamel cannot be regarded as self-similar across several levels, the assumption is used for two reasons: firstly, it is valid for at least the first two hierarchy levels, since the rods

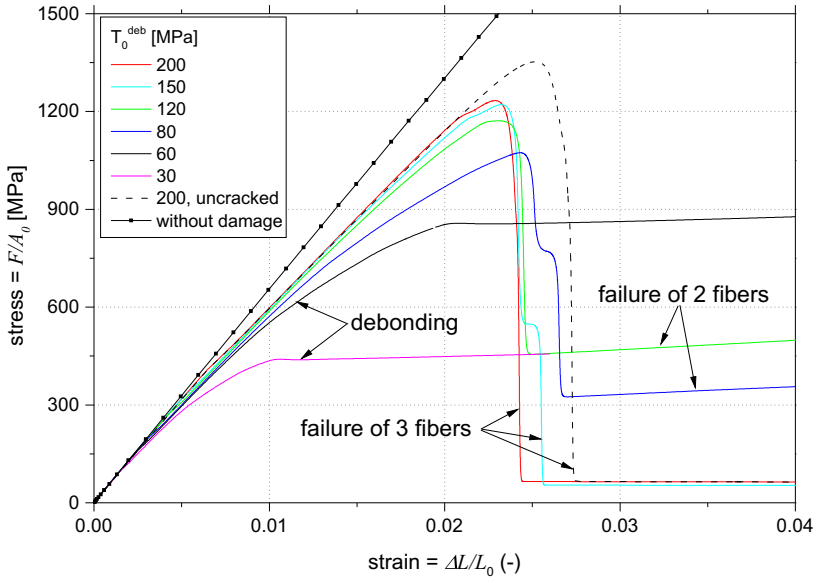

Fig. 5. Stress–strain behavior of the representative unit cell (first hierarchy level, precracked) under tensile loading in the fiber direction for various debonding strength values.

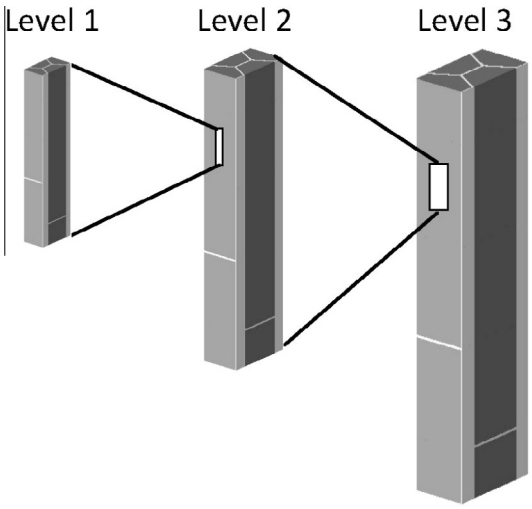

Fig. 6. Representative unit cell of the fibrous microstructure on three self-similar levels. Light grey: protein matrix. Dark grey: mineral.

have the same structure as the mineral fibers themselves (see Fig. 1)); and secondly, the method will be used in the future to characterize bioinspired materials, which can be produced in a self-similar manner, rather than enamel itself.

The material of the fiber under consideration differs from one scale to the next (and with this the fibers properties): on the first hierarchy level the fiber is modeled as HAp mineral, and on each higher level it consists of the homogenized composite of the level before.

On level 1, fiber and protein matrix are modeled explicitly as a heterogeneous composition of the original constituents, protein and HAp. On any higher hierarchy level the fiber consists of a homogenized fibrous microstructure and is assumed to be anisotropic hyperelastic. The constitutive model used for the representation of this behavior was first presented by Bonet and Burton [37] with four model parameters, then extended later for the complete transversely isotropic model (five parameters) (see e.g. Ref. [38,39]). Details of the model and parameter identification are presented in Ref. Appendix B.

In order to identify the fracture behavior on the second level, the representative unit cell results stated in Section 3 are used to extract the traction–separation law for the composite fiber, according to a procedure proposed in Ref. [40]. A similar method has been presented by other authors as well (see e.g. Ref. [41]). The basic ingredients of this homogenization procedure for damage are given in the following.

Based on the assumption that the total deformation $\mathbf{u}$ of the representative unit cell[3] consists of hyperelastic deformation $\mathbf{u}_{\mathrm{el}}$ and material separation $[\![\mathbf{u}]\!]$, the latter can be calculated by subtracting the elastic deformation, i.e. $[\![\mathbf{u}]\!] = \mathbf{u} - \mathbf{u}_{\mathrm{el}}$. The traction–separation law, $\mathbf{t}([\![\mathbf{u}]\!])$, can then be evaluated for each curve in Fig. 5. The result (in the present case for pure mode I separation) is shown in Fig. 7 for selected values of debonding strengths.

Internally, the traction vector, $\mathbf{t}$, is calculated using common damage mechanics representations, namely the undamaged (elastic) traction, $\mathbf{t}_{\mathrm{el}}$, is multiplied by a reduction factor $(1-d)$, with d being the internal damage variable evolving from 0 (undamaged) to 1 (fully damaged state):

$$\mathbf{t} = [1-d]\mathbf{t}_{\mathrm{el}} = [1-d]\overline{\mathbf{C}} \cdot [\![\mathbf{u}]\!] \tag{3}$$

[3] The normal component $\mathbf{u}_n$ is equal to the unit cell elongation, ΔL, which has been used in Fig. 5.

The damage is then adjusted such that, for a given stiffness $\overline{\mathbf{C}}$, the curves shown in Fig. 7 are retrieved.

From these traction–separation laws, one can extract some basic features of the fracture behavior on the second level, where the fiber consists of 90 vol.% HAp and 10 vol.% protein. The damage of the composite is characterized by two main parameters: the maximum strength, T_0, and the fracture energy $\Gamma_0 = \int_{\delta=0}^{\delta_0} T\,\mathrm{d}\delta$, where δ_0 is the critical separation at which the material cannot transfer any stress (complete failure). These parameters strongly depend on the debonding strength, T_0^{deb}, of the hierarchical level below (that is, the interface between HAp fiber and protein matrix). A graph showing the maximum strength and the fracture energy of the composite fibers is given in Fig. 8. The three different fracture modes achieved in the simulations are clearly recognizable. The energy is almost constant for any fracture mode, but changes to a different level when the fracture mode changes. In contrast to this behavior, the maximum strength changes gradually and remains constant at its highest level, that is, when all fibers break.

5. Experimental validation and discussion

In addition to the microstructural characterization already mentioned in Section 2, microstructural experiments have been conducted by Schneider and co-workers [16,17] on several hierarchy levels. For the experimental validation conducted here, microcantilever beam experiments [16] representing the first level of hierarchy are used. These are small cantilevers extracted from inside a fiber-reinforced rod shown in Fig. 1a. The cantilever specimen is loaded by indentation with a three-face pyramidal Berkovich indenter. The finite element structure (Fig. 9b) has been generated to be used with the homogenized anisotropic hyperelastic material model outlined in Appendix B (for parameters see Eq. (B.2)), the loading is applied by modeling the geometry of the indenter explicitly and corresponding contact conditions. Cohesive elements have been inserted in the model at the plane where the cantilever ends. The traction–separation behavior is the homogenized one shown in Fig. 7.

The fracture stress of the enamel cantilevers was found to be $\sigma_f = 978 \pm 52$ MPa, the elastic modulus $E = 54 \pm 2$ GPa (based on three samples) [16]. The finite element simulation is used to reproduce these values with the identified parameters. Stress and strain were calculated by the following equations:

$$\sigma = \frac{12Fl^*}{bh^2}, \quad \epsilon = \frac{s_A h}{[l^*]^2}, \quad E = \frac{\sigma}{\epsilon} \tag{4}$$

The dimensions are b, h and l, i.e. the width, height and length of the cantilever beam. l^* is the loading distance (from the support to the loading tip) and s_A is the displacement at the corner point at the same distance as the indenter (point A in Fig. 9b).

The simulations of the cantilever were conducted with different traction–separation laws for the fiber corresponding to results on level 1. The stress–strain curves calculated for these simulations are shown in Fig. 10, together with the experimental data. The response of the specimen in the experiment is linear only up to a stress of approx. 500 MPa. The subsequent nonlinearity, which is due to microdamage and debonding, should also be reproduced by the simulation.

The simulation without damage already shows that the stiffness of the specimen is slightly underestimated. The initial stiffness of the hyperelastic simulation is $E = 47.5$ GPa, which is still higher than the stiffness in the compression tests taken from Ref. [17] (shown additionally in Fig. 10 for information). This effect might be caused by a tension–compression asymmetry, which our hyperelastic model does not account for. On the other hand, the Young's

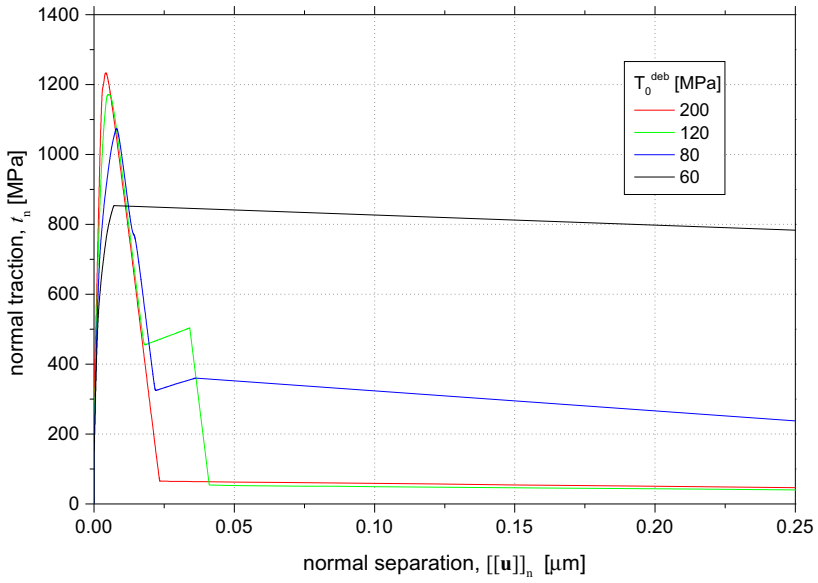

Fig. 7. Results of the first level, precracked RUC, transferred into traction–separation laws by subtracting the elastic deformation from the stress–strain curve shown in Fig. 5, $[\![\mathbf{u}_n]\!] = \Delta L - (\Delta L)_{el}$.

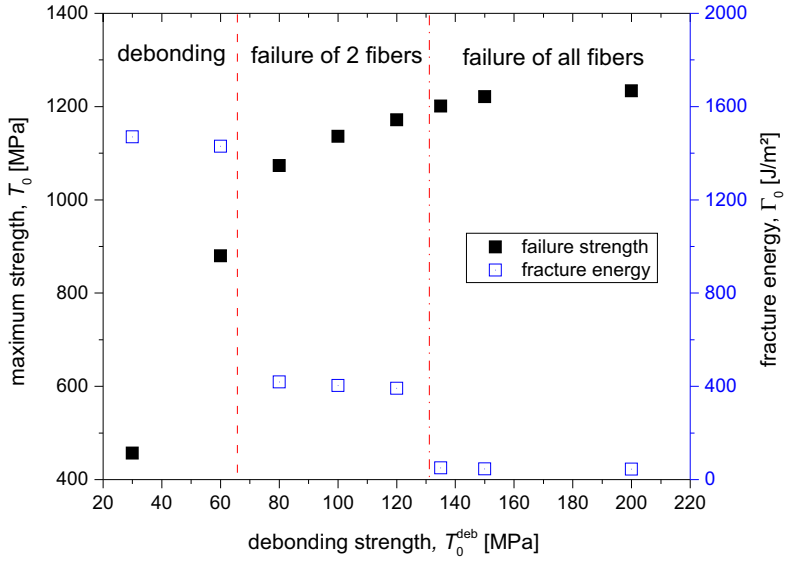

Fig. 8. Failure strength and fracture energy of the precracked representative unit cell under uniaxial tensile straining in fiber direction, depending on the debonding strength. The transition of the failure mechanism is clearly visible by the change in fracture energy, while the failure strength is only gradually affected.

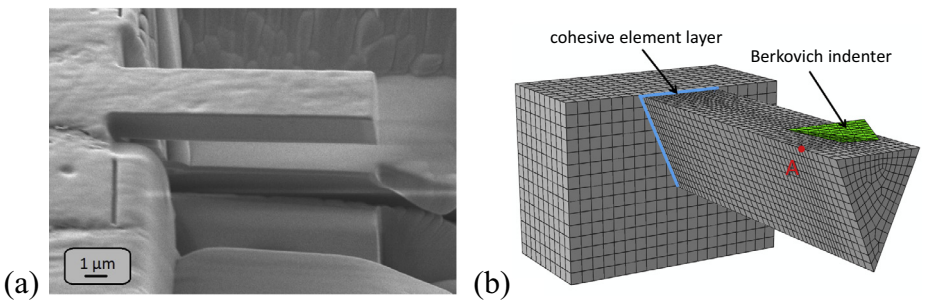

Fig. 9. Microcantilever beam. (a) Focused ion beam fabricated specimen (cross-section: 4.15 × 4.84 µm, length 15.75 µm); (b) corresponding simulation, including the Berkovich indenter. The blue line indicates the plane of cohesive elements.

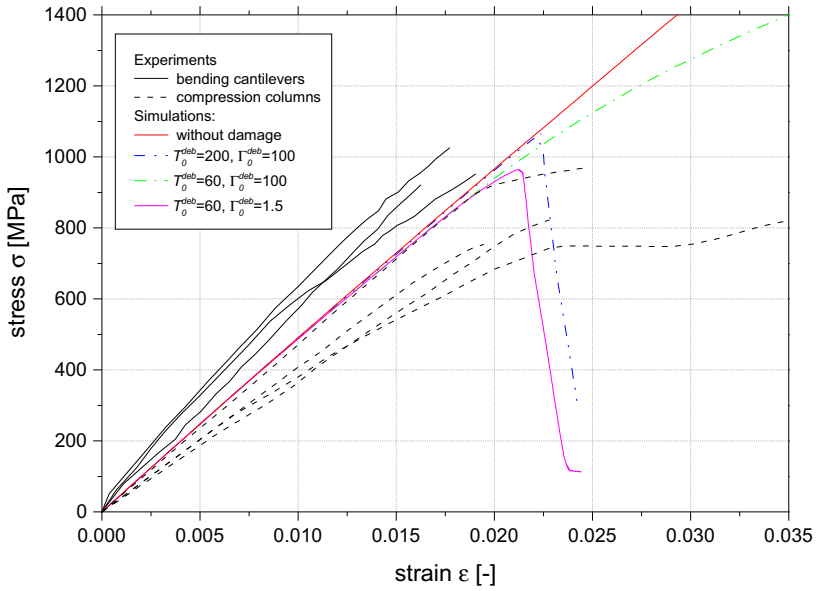

Fig. 10. Stress–strain results of the microcantilever beam: comparison between simulation and experiment. The data for the microcantilever beam experiments are taken from Ref. [16], the compression test data of the intra-rod columns from Ref. [17]. The non-linear stress–strain response is captured well for a cohesive debonding strength $T_0^{\text{deb}} = 60$ MPa.

modulus of both types of experiment and the simulation are in close agreement with other tests performed by nanoindentation (see e.g. Ref. [29,42]), where significantly higher values have been measured.

The nonlinearity in the experimental stress–strain behavior due to microcracking and damage in the protein, which starts well before fracture, can be captured by the simulation if the debonding strength $T_0^{\text{deb}} = 60$ MPa, identified as the most reasonable one in Section 3.2 is used (see Fig. 10). However, with a debonding energy $\Gamma_0^{\text{deb}} = 100\,\text{J/m}^2$ (the value used in Ref. [25]), the simulated strength of the beam ($\sigma_f = 1620$ MPa, which is outside the graph area) is much higher than the experimental value (between 920 and 1020 MPa). Therefore, this test is used to adjust the debonding energy in order to meet the experimental strength. Note that this quantity could not be identified by any simulation in the previous sections.

As a result of this identification, a significantly reduced debonding energy $\Gamma_0^{\text{deb}} = 1.5\,\text{J/m}^2$ leads to a very close agreement between simulation and experiment, as shown in Fig. 10. The maximum strength $\sigma_f = 965$ MPa is well inside the range of experimental values. Moreover, the general stress–strain behavior is well captured by the simulation.

The fracture strength of a larger debonding strength, $T_0^{\text{deb}} = 200$ MPa (this is the value used in Ref. [25]), is $\sigma_f = 1050$ MPa, which matches the experimental value quite well (see the additional curve in Fig. 10); however, the response of the simulated cantilever is linear up to the maximum strength, then drops steeply.

Even though it is a purely numerical issue, it is worth mentioning that a decrease of the debonding strength with all other parameters kept constant leads to a significant increase of the failure strength (distinguishable by comparing the two simulations with debonding energy $\Gamma_0^{\text{deb}} = 100\,\text{J/m}^2$ in Fig. 10. This effect was not visible in the simulation of the unit cell).

The simulation strategy used here is characerized by the use of purely phenomenological models, and the models do not capture such effects as tension–compression asymmetry, damage under compression or buckling. Further, in order to capture stochastic effects of irregularities, the simulations assume that generally every fourth fiber is 25% precracked. Despite this rather crude restriction, the agreement with the experiment is very good.

6. Conclusion

Dental enamel is a hierarchical and highly complex fiber-reinforced material which has a microstructure that has been experimentally investigated but is still not fully understood. It is not only of interest to biologists, veterinary and dentists, but also to engineers, as dental enamel possesses a very high fracture resistance due to its microstructure. In the case of dental enamel, learning from nature allows for the development of enhanced bioinspired ceramics.

A continuum mechanics based computational model for simulating the material response of dental enamel has been introduced. Various failure mechanisms are represented phenomenologically by cohesive interfaces. The model sheds light on the exact composition of the fiber-reinforced composite. While the experimental data reveals information on fracture mechanisms as well as material properties of the composite structure, it does not offer valuable clues on the material properties of the mineral fiber or the protein independently.

In the current work, we employed the idea of a bottom-up hierarchical structure and realized a complete scale separation in modeling in order to fill the gap between micromechanical based modeling and structural simulation of tooth fracture in the future. The model parameters have been identified with physical reasoning, leading to a microstructural simulation which is very close to the experimental results. This is worth mentioning in particular in consideration of the fact that the size of the initial crack (25% precracked in every fourth fiber) was just a rough estimate for any imperfection which may occur on the microscale. The nonlinear stress–strain response is captured well, and it transpires that the initial precrack plays only a minor role in the damage behavior of dental enamel.

The presented model discloses information on the optimal setup of a bioinspired fiber-reinforced composite. For the first time, simulations on consecutive hierarchy levels that take into account the material's damage behavior have been performed successfully

for a real biological material. As opposed to other studies, the type of failure mechanism is used not as an input in the simulations conducted but, rather, as a natural outcome. The cohesive zone model automatically provides information on how the damage evolves. The prediction of the failure is non-trivial, demanding a sophisticated material model on all hierarchy levels. Due to the complexity, a full resolution on all levels is computationally too costly, thus a homogenization was required. Finally the simulation verified the experiment by a rather complex material but simple geometric model that despite the fact that 25% of the initial fibers are initially precracked, the material still reaches a maximum strength of about 900 MPa before total failure.

The goal of our work is to understand the structure and property relationship of hierarchically structured biological materials, which could contribute bioinspired material research using the biological systems as models for engineering applications. This study contributes to the ongoing research towards an optimized design of a hierarchical advanced ceramics.

Acknowledgements

Partial financial support by ACE-Centre (Helmholtz-Zentrum Geesthacht, Germany) is gratefully acknowledged. Partial financial support by the German Research Foundation (DFG) via SFB 986 "M^3" (projects A6, B4 and B6) is also gratefully acknowledged.

Appendix A. Model for size effect simulations

In order to get information on the size of the HAp fibers, the size effect of the maximum strength (cf. Fig. 3) was investigated in Section 3.2. For the investigation of the theoretical strength, breaking has to be the dominant failure mechanism and debonding of fibers had to be avoided. The RUC used in the other simulations contains fiber ends the influence of which would be too large during the investigation of the size effect of the maximum strength. Further, the influence of the precrack would also be too large. As a consequence, a fiber-reinforced microstructure with a larger number of infinitely long fibers is used for this particular study. Therefore, a mesoscale rod-like structure is generated containing several prismatic HAp fibers with a hexagonal cross-section and thin protein interlayers (see Fig. A.11). The central fiber is precracked by 30%. Besides the HAp material in the fiber and the protein material in the interlayer, two sets of cohesive surfaces with different parameters are introduced at the bottom end of the rod, one for fiber breaking, the other for protein failure. That is, the bottom plane, which serves as a symmetry plane, may break, but there is no debonding and the crack cannot turn away from that plane. The complete structure is loaded under tension (displacement controlled) and deforms elastically until the cohesive surfaces reach their cohesive strength.

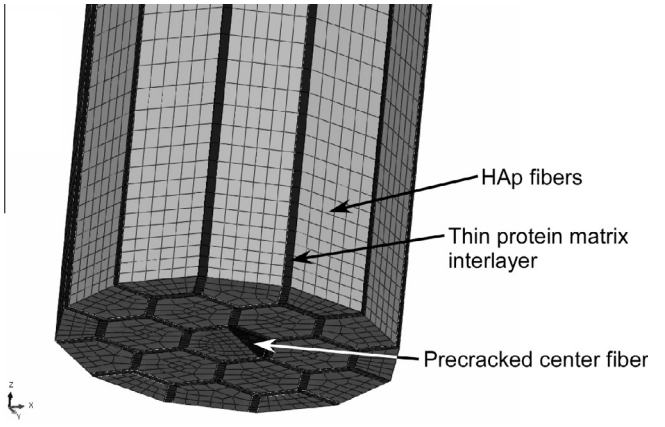

Fig. A.11. Mesoscale model of a rod-like structure containing several HAp fibers, the center one of which is 30% precracked.

Appendix B. Transversely isotropic hyperelastic material model

For the constitutive model of the homogenized material consisting of fibers surrounded by a thin protein layer, an invariant-based transverse isotropic hyperelastic model has been used. The constitution, first presented by Bonet and Burton [37] with four model parameters, and extended later for the complete transversely isotropic model (five parameters), e.g. in Ref. [38,39], utilizes a free energy density, ψ, based on two additional scalar invariants of the right Cauchy–Green strain tensor, **C**, which take the fiber direction vector **N** into account:

$$\psi = \psi_{\text{iso}} + \psi_{\text{trn}},$$
$$\psi_{\text{trn}} = [\alpha + \beta \ln J + \gamma[\mathbf{N}\cdot\mathbf{C}\cdot\mathbf{N} - 1]][\mathbf{N}\cdot\mathbf{C}\cdot\mathbf{N} - 1] - \frac{\alpha}{2}\left[\mathbf{N}\cdot\mathbf{C}^2\cdot\mathbf{N} - 1\right]. \tag{B.1}$$

Since the energy density is split additively into the isotropic and anisotropic parts, the model can be coupled to any isotropic hyperelastic material. Here, the isotropic part, ψ_{iso}, is assumed to be a neo-Hookean hyperelastic model. The properties of the material are given by three parameters, α, β and γ, along with the direction vector of the fiber, **N**, for the transversely isotropic and the Lamé parameters λ and μ for the isotropic part. This model is used for any higher hierarchy level $N > 1$, where the fibers consist of the fiber-reinforced composite of the level $N - 1$, that is, on level 2 the composite fiber consists of protein reinforced by HAp fibers (see Section 4). In addition, the model is used for the validation part (Section 5). It is worth noting that, according to the main assumption, the fiber direction does not change from level to level and thus only one extraordinary direction exists, such that the transversely isotropic material model can be used on every level.

While the parameters for protein and HAp have been proposed in Ref. [25], the parameters for the composite model must be identified using a homogenization strategy. Here, a numerical procedure based on the microstructural unit cell as shown in Fig. 6 is employed.

To identify the five hyperelastic model parameters, the representative unit cell already used in Section 3.2, but without a precrack, was loaded in six different displacement-ontrolled load cases, as shown in Fig. B.12: normal tensile loading (unidirectional strain) in three directions and shear loading in three directions applied to one face each. The other faces are stress free. The boundary conditions applied in these cases are periodic constraints.

From the applied load cases, the five parameters for the homogenized material of hierarchy level 1 are identified as follows:

λ	α	β	γ	μ
4315 MPa	300 MPa	368.75 MPa	6266.875 MPa	5400 MPa

(B.2)

The comparison between the representative unit cell and a single element with the constitutive model shows that the anisotropic material model can represent the unit cell deformation very well, the error always being below 5%.

Appendix C. Figures with essential colour discrimination

Certain figures in this article, particularly Figs. 3, 5, 7–10, B.12 are difficult to interpret in black and white. The full color images can be found in the on-line version, at http://dx.doi.org/10.1016/j.actbio.2014.11.036.

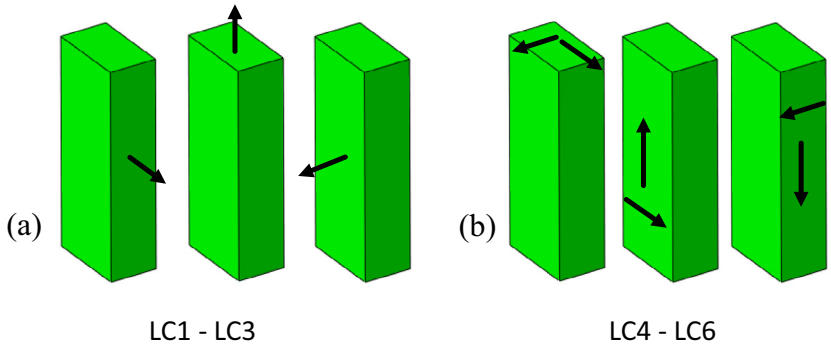

Fig. B.12. Principle sketch of the unit cell loaded in six different load cases. (a) Normal tensile loading in each direction, (b) shear loading.

References

[1] Nanci A. Ten Cate's oral histology: development, structure, and function. Elsevier Health Sciences; 2007.
[2] Tancred DC, McCormack BAO, Carr AJ. A quantitative study of the sintering and mechanical properties of hydroxyapatite/phosphate glass composites. Biomaterials 1998;19(19):1735–43.
[3] Kumar A, Biswas K, Basu B. On the toughness enhancement in hydroxyapatite-based composites. Acta Mater 2013.
[4] Gao H, Ji B, Jäger I, Arzt E, Fratzl P. Material becomes insensitive to flaws at the nanoscale: lessons from nature. Proc Natl Acad Sci 2003;100:5597–600.
[5] Wang J, Shaw LL. Nanocrystalline hydroxyapatite with simultaneous enhancements in hardness and toughness. Biomaterials 2009;30(34):6565–72.
[6] Veljović DJ, Jokić B, Petrović R, Palcevskis E, Dindune A, Mihailescu IN, et al. Processing of dense nanostructured hap ceramics by sintering and hot pressing. Ceram Int 2009;35(4):1407–13.
[7] Ang S, Bortel E, Swain M, Klocke A, Schneider G. Size-dependent elastic/inelastic behavior of enamel over millimeter and nanometer length scales. Biomaterials 2010;31:1955–63.
[8] Ang S, Schulz A, Pacher Fernandes R, Schneider G. Sub-10-micrometer toughening and crack tip toughness of dental enamel. J Mech Behav Biomed Mater 2011;4:423–32.
[9] Eimar H, Ghadimi E, Marelli B, Vali H, Nazhat SN, Amin WM, et al. Regulation of enamel hardness by its crystallographic dimensions. Acta Biomater 2012;8(9):3400–10.
[10] Maas MC, Dumont ER. Built to last: the structure, function, and evolution of primate dental enamel. Evol Anthropol Issues News Rev 1999;8(4):133–52.
[11] Koenigswald WV, Clemens WA. Levels of complexity in the microstructure of mammalian enamel and their application in studies of systematics. Scanning Microsc 1992;6:195–217.
[12] Bajaj D, Arola D. On the r-curve behavior of human tooth enamel. Biomaterials 2009;30:4037–46.
[13] Bajaj D, Arola D. Role of prism decussation on fatigue crack growth and fracture of human enamel. Acta Biomater 2009;5(8):3045–56.
[14] Yahyazadehfar M, Bajaj D, Arola DD. Hidden contributions of the enamel rods on the fracture resistance of human teeth. Acta Biomater 2012.
[15] Bechtle S, Habelitz S, Klocke A, Fett T, Schneider G. The fracture behaviour of dental enamel. Biomaterials 2010;31(2):375–84.
[16] Bechtle S, Özcoban H, Lilleodden E, Huber N, Schreyer A, Swain M, et al. Hierarchical flexural strength of enamel: transition from brittle to damage-tolerant behaviour. J R Soc Interf 2013:1265–74.
[17] Yilmaz E, Bechtle S, Özcoban H, Schreyer A, Schneider G. Fracture behavior of hydroxapatite nanofibers in dental enamel under micropillar compression. Scr Mater 2012:404–7.
[18] Gao H. Application of fracture mechanics concepts to hierarchical biomechanics of bone and bone-like materials. Int J Fract 2006;138:101–37.
[19] Zhang Z, Zhang Y-W, Gao H. On optimal hierarchy of load-bearing biological materials. Proc R Soc B Biol Sci 2011;278:519–25.
[20] Sen D, Buehler MJ. Structural hierarchies define toughness and defect-tolerance despite simple and mechanically inferior brittle building blocks. Sci Rep 2011;1:1–17.
[21] Bekah S, Rabiei R, Barthelat F. The micromechanics of biological and biomimetic staggered composites. J Bionic Eng 2012;9:446–56.
[22] Spears IR. A three-dimensional finite element model of prismatic enamel: a re-appraisal of the data on the young's modulus of enamel. J Dent Res 1997;76:1690–7.
[23] Bar-On B, Wagner HD. Enamel and dentin as multi-scale bio-composites. J Mech Behav Biomed Mater 2012;12:174–83.
[24] An B, Wang R, Zhang D. Role of crystal arrangement on the mechanical performance of enamel. Acta Biomater 2012;8(10):3784–93.
[25] Bargmann S, Scheider I, Xiao T, Yilmaz E, Schneider GA, Huber N. Towards bio-inspired engineering materials: modeling and simulation of the mechanical behavior of hierarchical bovine dental structure. Comput Mater Sci 2013;79:390–401.
[26] Barani A, Keown AJ, Bush MB, Lee JJ-W, Chai H, Lawn BR. Mechanics of longitudinal cracks in tooth enamel. Acta Biomater 2011;7(5):2285–92.
[27] Scheider I, Chen Y, Hinz A, Huber N, Mosler J. Size effects in short fibre reinforced composites. Eng Fract Mech 2013;100:17–27.
[28] Scheider I, Xiao T, Huber N, Mosler J. On the interaction between different size effects in fibre reinforced pmma: towards composites with optimised fracture behaviour. Comput Mater Sci 2013;80:35–42.
[29] Habelitz S, Marshall SJ, Marshall Jr GW, Balooch M. Mechanical properties of human dental enamel on the nanometre scale. Arch Oral Biol 2001;46(2):173–83.
[30] Han L, Wang L, Song J, Boyce M, Ortiz C. Direct quantification of the mechanical anisotropy and fracture of an individual exoskeleton layer via uniaxial compression of micropillars. Nano Lett 2011;11(9):3868–74.
[31] Daculsi G, Menanteau J, Kerebel LM, Mitre D. Length and shape of enamel crystals. Calcif Tissue Int 1984;36(1):550–5.
[32] Arruda E, Boyce M. A three-dimensional constitutive model for the large stretch behavior of rubber elastic materials. J Mech Phys Solids 1993;41(2):389–412.
[33] Wu X, Levenston ME, Chaikof EL. A constitutive model for protein-based materials. Biomaterials 2006;27(30):5315–25.
[34] Mosler J, Scheider I. A thermodynamically and variationally consistent class of damage-type cohesive models. J Mech Phys Solids 2011;59:1647–68.
[35] Dastjerdi AK, Pagano M, Kaartinen MT, McKee MD, Barthelat F. Cohesive behavior of soft biological adhesives: experiments and modeling. Acta Biomater 2012;8:3349–59.
[36] Rabiei R, Bekah S, Barthelat F. Failure mode transition in nacre and bone-like materials. Acta Biomater 2010;6:4081–9.
[37] Bonet J, Burton AJ. A simple orthotropic, transversely isotropic hyperelastic constitutive equation for large strain computations. Comput Methods Appl Mech Eng 1998;162:151–64.
[38] Wu L, Tjahjanto D, Becker G, Makradi A, Jerusalem A, Noels L. A micro-meso-model of intra-laminar fracture in fiber-reinforced composites based on a discontinuous galerkin/cohesive zone method. Eng Fract Mech 2013;104:162–83.
[39] Somer DD, Peric D, de Souza Neto EA, Dettmer WG. On the characterisation of elastic properties of long fibre composites using computational homogenisation. Comput Mater Sci 2014;83:149–57.
[40] Scheider I. Derivation of separation laws for cohesive models in the course of ductile fracture. Eng Fract Mech 2009;76:1450–9.
[41] Nguyen VP, Stroeven M, Sluys LJ. An enhanced continuous-discontinuous multiscale method for modeling mode-i cohesive failure in random heterogeneous quasi-brittle materials. Eng Fract Mech 2012;79:78–102.
[42] Chai H. On mechanical properties of tooth enamel under spherical indentation. Acta Biomater 2014;10(11):4852–60.